Research Article
doi.org/10.1002/cmtd.202400058

Chemistry Europe
European Chemical Societies Publishing

www.chemistrymethods.org

Revealing the Mechanism and Kinetics of Fe_5C_2 Formation From Ferrous Oxalate under CO_2 Fischer-Tropsch Conditions Using Time-Resolved In Situ X-Ray Absorption Spectroscopy

Elizaveta A. Fedorova,*[a] Aleksandr Fedorov,[b] Dmitry E. Doronkin,[c] David Linke,[b] Christoph Kubis,[a] Angelika Brückner,[a] and Evgenii V. Kondratenko*[a]

The fundamentals of in situ formation of iron carbides are required for the tailored design of Fe-based catalysts for the efficient conversion of CO_2 to higher hydrocarbons. Herein, time-resolved in situ X-ray absorption spectroscopy has been used to elucidate the mechanism of the formation of Fe_5C_2 from ferrous oxalate (FeC_2O_4) at 350 °C using a $H_2/CO = 3$ reaction feed. Regardless of the kind of alkali metal promoter and reaction pressure (1 or 7.5 bar), FeC_2O_4 is first decomposed to FeO followed by the conversion of the latter to Fe_5C_2. Further insights into the above transformations were derived by kinetic analysis using a Johnson–Mehl–Avrami–Erofeev–Kolmogorov model and kinetics-constrained neural ordinary differential equations method. Both approaches revealed that the formation of FeO at 1 bar follows a nucleation mechanism, while a diffusion mechanism has a higher contribution at 7.5 bar. The latter mechanism is valid for the conversion of FeO to Fe_5C_2 at both pressures. Alkali metal promoters were found to accelerate the rate of Fe_5C_2 formation. This rate decreases with increasing total pressure due to the stabilization of FeO.

Introduction

Ferrous oxalate dihydrate ($FeC_2O_4{\cdot}2H_2O$) is a versatile precursor used to produce various iron oxides, metallic iron, and iron carbides for different applications in medicine, solar water decomposition, magnetic materials, and catalysis.[1–4] The nature of the iron-containing products formed depends on the reaction atmosphere, in which it is treated.[5–7] For example, Fe_2O_3 nanoparticles are produced by decomposing $FeC_2O_4{\cdot}2H_2O$ in oxidizing atmospheres (air, O_2).[2,7–10] Nicholson found that this compound is extremely oxygen sensitive and its dehydration and decomposition might occur practically simultaneously in the temperature range of 150–230 °C.[11] The calcination conditions and morphology of $FeC_2O_4{\cdot}2H_2O$ influence the formation of α-Fe_2O_3 and/or γ-Fe_2O_3.[2,8–9,12–13]

In contrast to an oxidizing atmosphere, FeC_2O_4 is stable in vacuum or inert atmosphere. Thus, its decomposition and the dehydration of $FeC_2O_4{\cdot}2H_2O$ occur at different temperatures.[3,5–7,11,14] Decomposition to FeO with the formation of gas-phase CO and CO_2 starts in the temperature range of 300–360 °C.[5,7,10,15–17] As this iron oxide is unstable in this temperature range, it disproportionates to Fe and Fe_3O_4.[1,7,9–10] However, many authors mentioned that secondary reactions between Fe-containing phases and gases, e.g., H_2O, CO_2, CO, formed during the decomposition process take place.[3,15] For example, H_2O can oxidize FeO to Fe_3O_4.[9,15,18–20] CO is involved in the formation of Fe carbides.[3,21–23] The decomposition in an H_2-containing atmosphere proceeds via the formation of FeO followed by its disproportionation to Fe and Fe_3O_4.[1,24] Both iron oxides can be reduced to metallic Fe.

Since Fe_3O_4 and Fe carbides, which are active components of Fe-based catalysts used in CO_2 Fischer-Tropsch (CO_2-FT),[25–27] can be formed through simple thermal decomposition of $FeC_2O_4{\cdot}2H_2O$, this material was used for the preparation of CO_2-FTS catalysts.[4, 12,22–23,28–33] In addition, our group recently demonstrated that $FeC_2O_4{\cdot}2H_2O$ can be directly used for CO_2-FT.[30] The catalytically active phases are formed in situ. Such approach eliminates any catalyst pre-treatment steps. It was also shown that the spatial distribution of Fe-containing phases formed in situ depends on the kind of alkali metal promoter introduced to $FeC_2O_4{\cdot}2H_2O$ via impregnation with an aqueous solution of the respective carbonate. The fraction of Fe carbides in the spent (after CO_2-FTS) promoted catalysts increased in the order Li < Na < Rb < K < Cs. However, neither mechanistic nor

---

[a] *Department: Advanced Methods for Applied Catalysis, Institution: Leibniz Institute for Catalysis e. V. (LIKAT) Address, Rostock,*

[b] *Department: Catalyst Discovery and Reaction Engineering, Institution: Leibniz Institute for Catalysis e. V. (LIKAT), Rostock,*

[c] *Department: Catalysis and operando spectroscopy, Institution: Institute of Catalysis Research and Technology and Institute for Chemical Technology and Polymer Chemistry, Karlsruhe Institute of Technology (KIT), Karlsruhe,*

Correspondence: *Dr. Elizaveta A. Fedorova and Prof. Dr. Evgenii V. Kondratenko, Department: Advanced Methods for Applied Catalysis, Institution: Leibniz Institute for Catalysis e. V. (LIKAT) Address, Albert-Einstein Str. 29a, 18059 Rostock, .*
Email: elizaveta.fedorova@catalysis.de and evgenii.kondratenko@catalysis.de

Supporting Information for this article is available on the WWW under https://doi.org/10.1002/cmtd.202400058

kinetic studies of reaction-induced transformations of bare and promoted $FeC_2O_4·2H_2O$ were carried out.

Based on the above, the purpose of this study was to elucidate the mechanism of the formation of Fe-containing phases/species from $FeC_2O_4·2H_2O$ under CO_2-FTS conditions and to derive the kinetics of the individual steps. Such knowledge may be helpful in the design of catalysts based on this Fe-containing precursor. To achieve this, a family of materials based on $FeC_2O_4·2H_2O$ without or with an alkali metal (Li, Na, K, Rb or Cs) promoter were prepared and abbreviated as 0M/Fe, 0.005Li/Fe, 0.005Na/Fe, and 0.005K/Fe, 0.005Rb/Fe or 0.005Cs/Fe. The numbers stand for the atomic ratio of promoter/Fe. The dynamics of reaction-induced phase changes in these materials at 1 and 7.5 bar and 350 °C using a $CO_2/H_2=1/3$ feed was investigated by means of time-resolved in situ X-ray absorption spectroscopy (XAS). The obtained temporal profiles of the identified Fe-containing phases were evaluated to understand the mechanism and derive the kinetics of their formation.

Results and Discussion

Dehydration of $FeC_2O_4·2H_2O$ in He During Heating

Figure 1 shows the in situ XANES (a) and EXAFS (b) spectra of $FeC_2O_4·2H_2O$, which were measured during heating in He to 350 °C. The corresponding data on the promoted materials are presented in Figure S1. For all materials, some changes in the XANES spectra were observed, although the pre-edge peak at about 7112.5 eV did not change. Thus, the oxidation state of iron did not change and was 2+.[34] Based on the EXAFS spectra, the local environment of Fe^{2+} in these materials is very similar. Only changes in peak intensity are seen. As additional bonds such as Fe–O–Fe or Fe–Fe present in iron oxides or metallic Fe were not observed (Figure S2, Table S1), we can safely conclude that FeC_2O_4 did not start to decompose during heating in He. Using the spectra measured at 25 and 350 °C as references for $FeC_2O_4·2H_2O$ and FeC_2O_4, respectively, their linear combination analysis (LCA) was performed to visualize the dehydration process (Figure S3). The obtained fraction of FeC_2O_4 as a function of temperature is shown in Figure 1c. The temperature required to achieve 50 % dehydration of all samples is in the range of 137–150 °C, which is similar to that reported in previous studies dealing with the dehydration of $FeC_2O_4·2H_2O$.[3,11,15] No clear correlation between this parameter and the kind of alkali metal was established in this study.

Decomposition of FeC_2O_4 in CO_2+H_2

To elucidate the mechanism and derive the kinetics of the decomposition of FeC_2O_4 under conditions relevant to CO_2-FT, we performed in situ XAS experiments at 350 °C, 1 and 7.5 bar using a $H_2/CO_2=3$ feed. All materials were initially heated to this temperature in He to dehydrate $FeC_2O_4·2H_2O$ to FeC_2O_4. An increase in the intensity of the pre-edge peak at 7112.7 eV is visible in the XANES spectra of all samples tested at 1 bar (Figure 2a, Figures S4). Irrespective of the presence or the kind of alkali metal promoter, the XANES spectra recorded after 120 min on stream look similar to that of the Fe_5C_2 reference but are not identical (Figure 2b). The intensity of the pre-edge peak in the XANES spectra of 0.005Rb/Fe and 0.005Cs/Fe is lower compared to the Fe_5C_2 reference and other materials tested, probably due to the incomplete decomposition of FeC_2O_4 after 120 min. The pre-edge peak intensity in the XANES spectra of 0M/Fe, 0.005Li/Fe, 0.005Na/Fe, and 0.005K/Fe is same as for Fe_5C_2, but the position of the white line maximum is at 7129.6 eV as opposed to the 7131.8 eV in the reference spectrum. The reason might be explained by the formation of defective Fe_5C_2 with additional amorphous iron oxide on the surface (Figure S5).[35–36] The comparison of the EXAFS spectra after 120 min on reaction stream (Figure 2c) shows the same local environment of iron in the Fe_5C_2 reference and the 0M/Fe, 0.005Li/Fe, 0.005Na/Fe, and 0.005K/Fe samples with a difference in the peak intensities. The EXAFS fitting suggests the presence of the same Fe-C and Fe-C-Fe scattering in these samples as in Fe_5C_2 (Figure S6, Table S1). Thus, FeC_2O_4 in these samples should be almost completely decomposed to Fe_5C_2 (Figure S5, Table S1). On this basis, we used the XANES spectrum of FeC_2O_4 after 120 min on reaction stream as the refence spectrum representing Fe_5C_2 formed in situ for further LCA of the time-

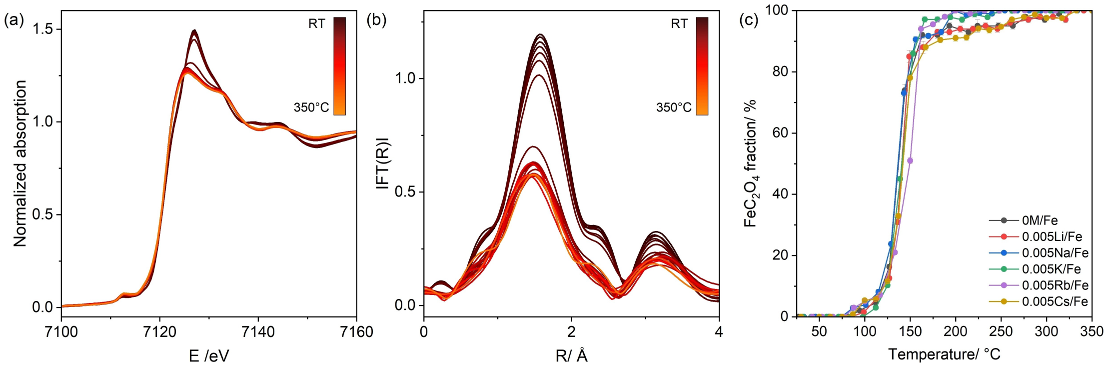

Figure 1. (a) The XANES and (b) EXAFS spectra of the 0M/Fe sample during heating in He to 350 °C. (c) The fraction of anhydrous FeC_2O_4 at different temperatures during heating in He to 350 °C. It was obtained by a linear combination analysis of the XANES spectra. The data are openly available in [37].

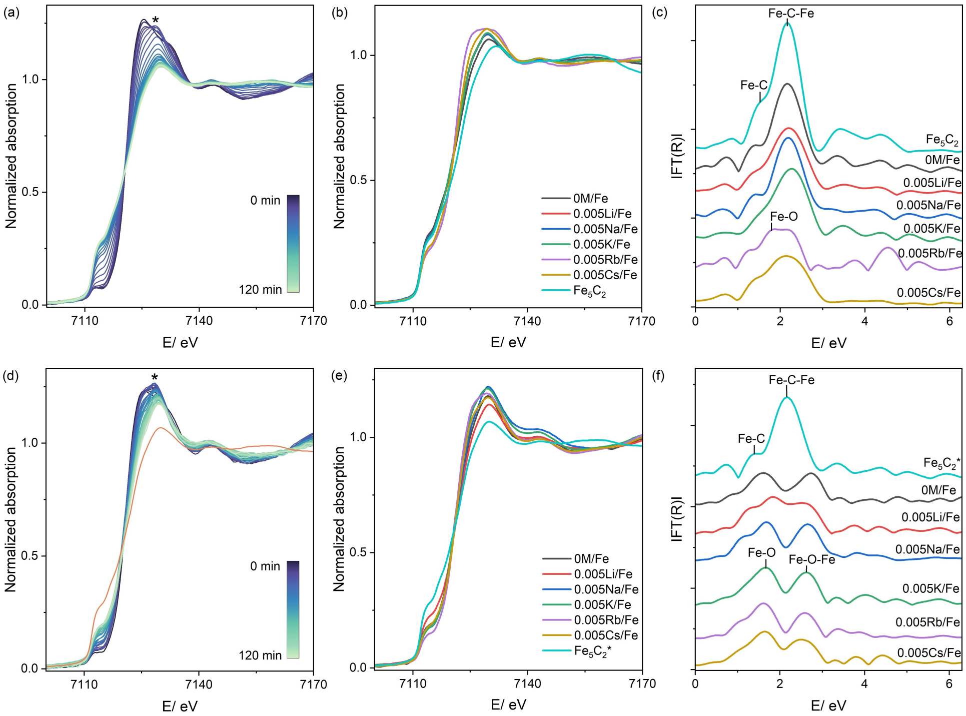

Figure 2. The XANES spectra of the 0M/Fe sample at 350 °C and (a) 1 bar or (d) 7.5 bar using a $H_2/CO_2 = 3$ reaction feed. The orange line represents the spectrum of Fe_5C_2* (the spectrum of the 0 M/Fe sample after 120 min treatment in He at 350 °C and 1 bar). (c, e) The XANES and (d, f) EXAFS spectra of different samples measured at room temperature after 120 min on H_2/CO_2 stream at 350 °C and (b, c) 1 bar or (e, f) 7.5 bar. The data are openly available in [37].

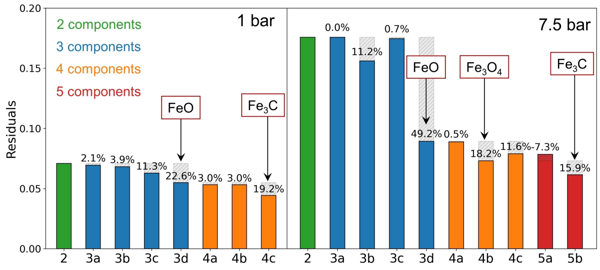

Figure 3. The mean residual values obtained by the linear fit of XANES data at 1 bar (left) and 7.5 bar (right) using different reference spectra. The percentage above each bar represents the relative reduction in residual values after adding a new component. The labels below the graph refer to the phases used for fitting: (2) – FeC_2O_4 and Fe_5C_2; the 3d component added to FeC_2O_4 and Fe_5C_2 is (3a) – Fe, (3b) – Fe_3O_4, (3c) – Fe_3C and (3d) – FeO; the 4th component added to FeC_2O_4, Fe_5C_2 and FeO is (4a) – Fe, (4b) – Fe_3O_4 and (4c) – Fe_3C; the 5th component added to FeC_2O_4, Fe_5C_2, FeO and Fe_3O_4 is (5a) – Fe and (5b) – Fe_3C. The data are openly available in [37].

resolved spectra of other materials. This reference material is abbreviated as Fe_5C_2*.

No complete conversion of FeC_2O_4 to Fe_5C_2 in all catalysts could be achieved even after 120 min on $H_2/CO_2 = 3$ stream at 7.5 bar (Figure 2d–f, Figure S7-S8, Table S1). Based on the intensity of the pre-edge peak of the XANES spectra after 120 min of stream (Figure 2e), the highest and lowest amount of Fe_5C_2 should be present in the 0.005Li/Fe and 0.005Rb/Fe samples, respectively.

It is worth mentioning that an additional peak at 7128.5 eV appeared in the XANES spectra during the decomposition process (Figure 2a, d) indicating the formation of intermediate phases. To identify the number of independent compounds in the data set obtained, we applied principal component analysis (PCA).[38–40] The scree plot[39–40] and the factor indicator function (IND) suggested by Malinowski[41] were used to analyse the PCA data (Figure S9). The obtained number of independent components is presented in Table S2. The analysis with the scree plot suggests that at least 3 components are needed to describe the data set for all samples, whereas a higher number (up to 7–8) is predicted by the IND function. However, the latter can overestimate the number of compounds as reported in a previous study.[40] Due to the complexity and limitations of PCA and, in particular, its data interpretation,[38] we applied the linear fit of the XANES data set measured at one pressure with different numbers of reference spectra.[42] Figure 3 shows the dependencies between the mean value of the residuals and the number/type of reference spectra used for the fit. On this basis, FeO was identified as the best additional component formed at both 1 and 7.5 bar. The formation of FeO as the first step of FeC_2O_4 decomposition is discussed in the literature.[5, 7, 10, 15–17] For the data measured at 1 bar, the addition of metallic Fe or Fe_3O_4 did not lead to a significant improvement. However, the inclusion of Fe_3C led to a moderate residual decrease of 19.2 %, which may indicate the formation of Fe_3C as an intermediate phase. In the case of tests at 7.5 bar, the addition of metallic Fe did not result in a decrease in the residual. However, the formation of Fe_3O_4 and Fe_3C cannot be excluded.

To illustrate the time-resolved evolution of the conversion of FeC_2O_4 to Fe_5C_2, the XANES spectra of each catalyst in

Figures S4 and S7 were fitted by LCA using the reference spectra of FeC_2O_4, FeO, Fe_3C, Fe_5C_2* and Fe_3O_4 (Figure 4, Figure S10). Irrespective of the kind and presence of alkali metal promoter and the reaction pressure, the first step in the decomposition of FeC_2O_4 is the formation of FeO (equation 1). For all samples, a small fraction of Fe_3C was also identified during the decomposition. We suppose that FeO is further transformed to Fe_3C and then to Fe_5C_2 under reaction conditions probably according to equations 2 and 3.

$$FeC_2O_4 \rightarrow FeO + CO_2 + CO \tag{1}$$

$$3FeO + CO_2 + 5H_2 \rightarrow Fe_3C + 5H_2O \tag{2}$$

$$5Fe_3C + CO_2 + 2H_2 \rightarrow 3Fe_5C_2 + 2H_2O \tag{3}$$

In contrast to tests at 1 bar, the fraction of FeO in tests at 7.5 bar reached a certain value after a short time on $H_2/CO_2 = 3$ stream and changed little with a further increase in the time. The time-on-stream changes in the fraction of the Fe_5C_2 phase at this pressure are also slower in comparison to the tests at 1 bar. Although FeO is not stable in an oxidizing atmosphere at 350 °C,[43] our experiments demonstrate that this phase can be stabilized at this temperature when using an $H_2/CO_2 = 3$ feed at 7.5 bar. This may be explained by the stabilizing effect of water.[44–45] This product is formed by reverse water gas shift reaction involving CO_2. For this reason, we put forward that water also lowers the conversion of FeO to iron carbide.

After more than 30 minutes on reaction stream at 7.5 bar, Fe_3O_4 started to be formed. Its formation could occur via two routes: the disproportionation of FeO to Fe and Fe_3O_4, and the oxidation of FeO by water (equation 4). We suppose that the latter route is more likely because the formation of metallic Fe, if the disproportionation occurred, was not supported by linear fit of XANES data (Figure 3).

$$3FeO + H_2O \rightarrow Fe_3O_4 + H_2 \tag{4}$$

Kinetic Modelling of Decomposition of FeC_2O_4 in $CO_2 + H_2$

First, we applied the traditional kinetic approach using Johnson–Mehl–Avrami–Erofeev–Kolmogorov (JMAEK) model (equations 7–8 in section **Kinetic modeling** in the Experimental part) to describe the first step of FeC_2O_4 decomposition, i.e., the formation of FeO (equation 1). This model has been successfully applied in many previous studies dealing with different compounds.[46–50] To refine the steps of the formation of FeO and its consecutive conversion to iron carbide during FeC_2O_4

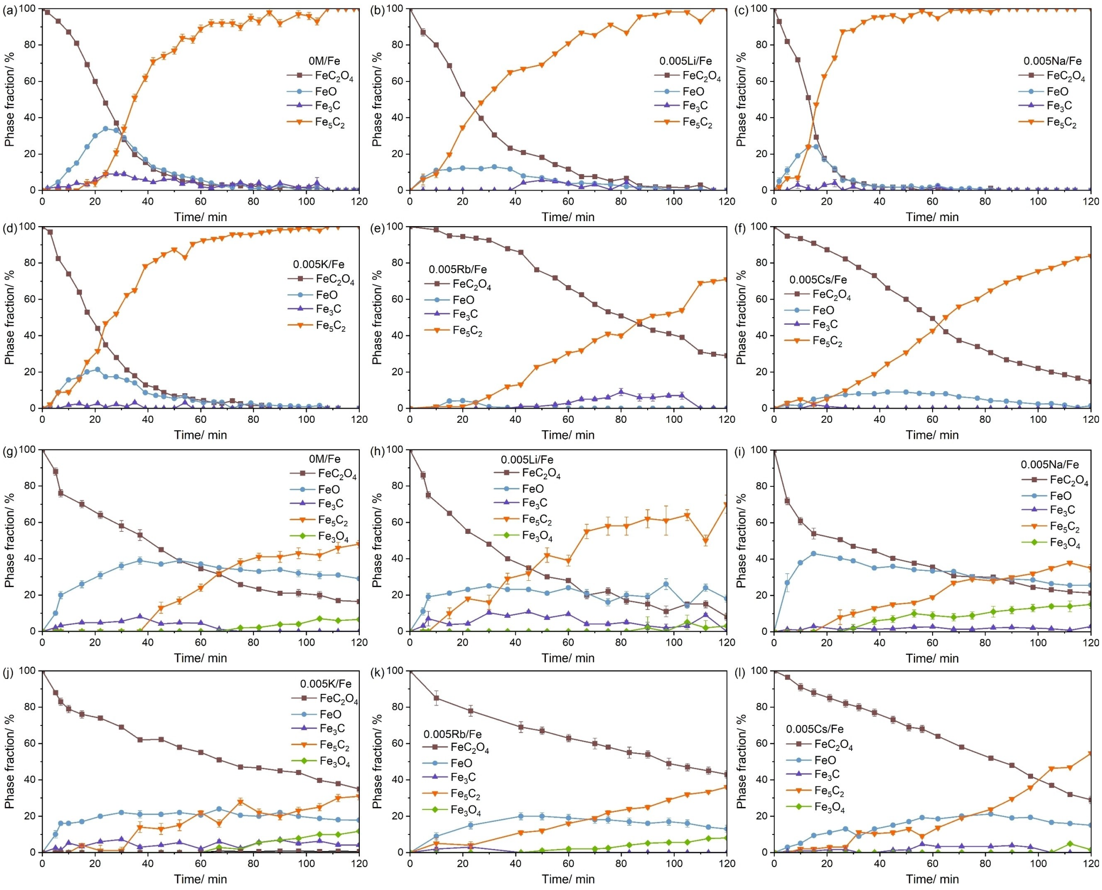

Figure 4. The time-resolved profiles of fractions of Fe-containing phases formed during the treatment of (a, g) 0M/Fe, (b, h) 0.005Li/Fe, (c, i) 0.005Na/Fe, (d, j) 0.005K/Fe, (e, k) 0.005Rb/Fe, and (f, l) 0.005Cs/Fe at 350 °C and (a-f) 1 bar or (g-l) 7.5 bar in a $H_2/CO_2 = 3$ mixture. The data are openly available in [37].

decomposition, kinetic modelling using ordinary differential equations (ODEs) was applied (see section **Kinetic modeling** in the Experimental part). To validate the latter approach, the rates of the formation of FeO, the first step of the decomposition of FeC_2O_4 (equation 11), obtained by these two approaches were calculated and compared.

The parameter *n* in equation 7 depends on the nucleation and growth mechanism and/or dimensionality of crystal growth. When *n* is larger than 1, the nucleation process largely contributes to the reaction studied. This contribution is less pronounced for *n* values below 1. Thus, the phase transformation is determined by the diffusion-controlled growth of the new phase. The *n* and *k* parameters were estimated by a linear regression fitting of the experimental data (the conversion values α were calculated from the fraction of FeC_2O_4 in Figure 4) in the Sharp-Hancock coordinates (equation 9 in section **Kinetic modeling** in the Experimental part) (Figure 5a,b, S11). The obtained rate constant of the conversion of FeC_2O_4 to FeO is presented in Tables S3, while the respective *n* values are presented in Figure 5c. For all materials tested at 1 bar, the latter are larger than 1 (1.4-2.2) indicating that the nucleation mechanism plays an important role in the decomposition of FeC_2O_4. When this reaction was investigated at 7.5 bar, the *n* values of all catalysts decreased and became less than 1 in the case of the 0M/Fe, 0.005Li/Fe, 0.005Na/Fe, 0.005K/Fe and 0.005Rb/Fe catalysts. Thus, the decomposition reaction in these materials at elevated pressures should be controlled by the diffusion growth. The nucleation process still contributes to the FeC_2O_4 decomposition in the 0.005Cs/Fe catalysts since *n* is 1.4, which is larger than 1.

To obtain the kinetic parameters of the conversion both of FeC_2O_4 to FeO (equation 1) and FeO to iron carbides (Fe_xC_y, equations 2 and 3), a kinetic-constrained neural ODE approach was used to fit the in situ XAS data in Figure 4. Three models (M−1, M−2 and M−3 (see section **Kinetic modelling** in the Experimental section) were tested for their ability to describe the complete transformation profile. The M−2 was found to fit the experimental data at 1 and 7.5 bar better compared to M−1 (Table S4, Figures S12-S13). It indicates that the overall rate of FeC_2O_4 decomposition depends not only on the fraction of ferrous oxalate but also on the fraction of FeO, which is significantly higher at 7.5 bar than at 1 bar. Probably, FeO may cover FeC_2O_4 thus resulting in diffusion limitations for removing gaseous CO and CO_2 during FeC_2O_4 decomposition. The dependence of the FeC_2O_4 decomposition rate on the FeO amount at 7.5 bar is more pronounced because of the stability of this oxide. However, the data could be better described by model M−3 (Table S4, Figure S14). This model considers the influence of the promoters on the individual reactions in the course of FeC_2O_4 decomposition suggesting different reaction mechanisms. This agrees with the analysis of the decomposition using with the JMAEK model (Figure 5c); for example, at 7.5 bar the nucleation mechanism ($n \geq 1$) prevails in the case of the 0.005Cs/Fe sample, while the diffusion mechanism ($n < 1$) is valid for other samples.

To validate the results obtained with the neural ODE models, we calculated the rate of conversion of FeC_2O_4 to FeO at a 50% conversion of FeC_2O_4 using the kinetic parameters obtained by these models and compared with the data obtained by the traditional JMAEK model (equations 7 and 8). The corresponding rate values are shown in Figure S15. The ODE results obtained with M−3 have a good convergence with those obtained by the classical approach ($R^2 = 0.99323$ and 0.92457, Figure S15). The other neural ODE models also show good convergence for the 1 bar data, but not for the 7.5 bar data (Figure S15), probably, due to their failure to describe the experimental data correctly (Figure S12, S13). The above analysis suggests that the neural ODE approach provides similar results as the classical modelling and thus may be used to determine kinetic parameters of solid-state transformations/conversion. Moreover, neural ODE models are not limited to a single reaction but could extract information about investigate the conversion of FeO to iron carbide that occurs in parallel with the decomposition of FeC_2O_4 to FeO.

To analyze the effect of the kind of alkali metal promoter on the rates of FeC_2O_4 and FeO decomposition, the initial rates, where only the reagent is present, were estimated using the obtained models (Table S5; Figure 6a,b). The fractions of FeC_2O_4 (x_1) and FeO (x_2) were 1 and 0 for the first reaction (FeC_2O_4 to FeO) but 0 and 1 for the second reaction (FeO to Fe_xC_y). For all samples, the rate of the first reaction increases with increasing total pressure (Figure 6a,c). At 1 bar, the catalysts can be

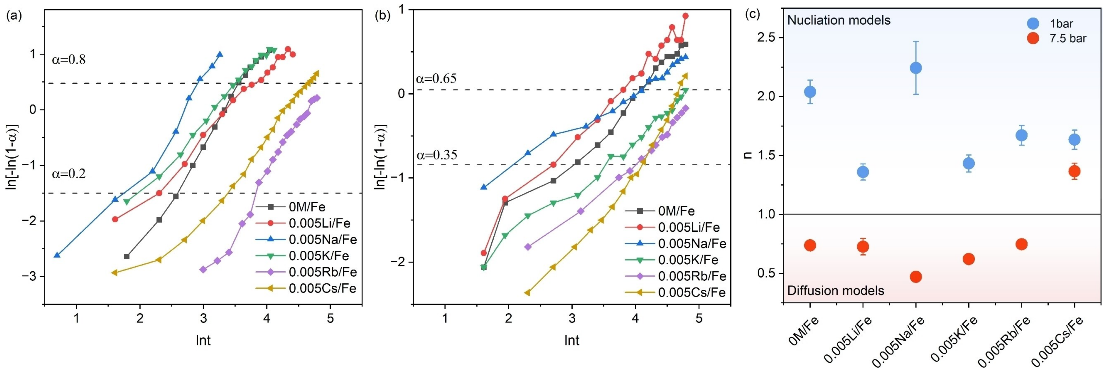

Figure 5. The Sharp-Hancock plot of FeC_2O_4 decomposition in different catalysts at 350 °C and (a) 1 or (b) 7.5 bar. The conversion (α) of FeC_2O_4 was obtained from the fraction of the FeC_2O_4 phase as determined from in situ XAS experiments. (c) The values of the parameter *n* obtained by linearization of the Sharp-Hancock plotted data in (a) and (b). The fits are shown in Figure S10. The data are openly available in [37].

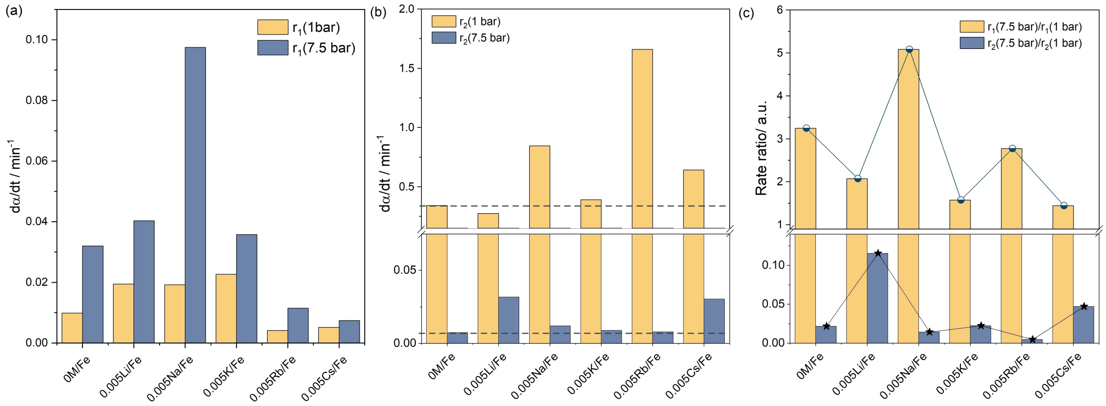

Figure 6. The initial rates of (a) FeC_2O_4 decomposition to FeO and (b) FeO conversion to Fe_xC_y (Fe_3C and Fe_5C_2) for different samples tested at 1 and 7.5 bar. (c) The ratios of r_1/r_1 and r_2/r_2 at 7.5 bar to 1 bar. The data are openly available in [37].

ordered in terms of their decomposition activity as follows: 0.005Na/Fe $\approx$0.005Li/Fe $\approx$0.005K/Fe $>$0M/Fe $>$0.005Cs/Fe $\approx$0.005Rb/Fe. This tendency is almost maintained at 7.5 bar, with only 0.005Na/Fe showing the highest decomposition rate. The dependence of the FeC_2O_4 decomposition rates on alkali metals could be due to the combination of different promotional effects of alkali metals such as electron donation, changes in surface basicity, active facets stabilization, different mobility of alkali metals, etc.[51–52] Probably, the alkali metals could interact with the oxalate group and form $MC_2O_4^-$ fragments (M = alkali metal) during the decomposition. Jestilä J. S. et. al[53] showed that such intermediates have different structures and length of M-O bonds. It was shown that the stronger interactions of Li, Na, and K with the oxygens in the oxalate fragment could lead to the elongation of the C-C bond, and, probably, its faster rupture during FeC_2O_4 decomposition. Meanwhile, Rb and Cs in staggered configurations with the oxalate fragment are characterized by three longer M-O bonds providing a shorter C-C bond, which might lead to higher stability of the oxalate and a lower rate of FeC_2O_4 decomposition compared to the unpromoted sample.

The predicted acceleration of the initial rate (Figure 6a, 6c) and deceleration of the rate at 50% FeC_2O_4 conversion (Figure S15) with increasing pressure could be explained by the difference in the reaction mechanism. For example, in the case of the diffusion mechanism, the initial rate is higher than the rate at higher conversion degrees (Table S3). The nucleation mechanism is characterized by a low initial nucleation rate at the beginning but a further acceleration as the reaction progresses.[54] According to the JMAEK model (Figure 5c), the decomposition mechanism depends on pressure. This model cannot, however, predict whether and how the mechanism changes with rising conversion. To provide some hints in this regard, we used the neural ODE model to check for possible dependencies between the n and α values for both FeC_2O_4 decomposition to FeO and FeO conversion to Fe_xC_y (Figure S16).

For all samples tested, the n values for the first reaction at 1 bar are larger than 1 in the entire α range. Thus, the nucleation mechanism should dominate the decomposition process. The n value of the samples measured at 7.5 bar is lower than at 1 bar, and the $n$values of the 0M/Fe, 0.005Li/Fe, 0.005Na/Fe, 0.005K/Fe, and 0.005Rb/Fe samples are lower than 1 for almost the entire α range indicating the prevalence of the diffusion mechanism. These data also correlate with n values estimated by JMAEK model (Figure 5c) pointing to the correct data fitting by the neural ODE approach.

For the conversion of FeO to Fe_xC_y in all materials, the n values are lower than 1 (except for 0.005Cs/Fe at 7.5 bar with the n values in the 0.97-1.10 range) indicating the predominance of the diffusion mechanism at ambient and elevated pressures (Figure S16c,d). All promoted samples have higher initial conversion rate at 1 bar and 7.5 bar than their unpromoted counterpart (except 0.005Li/Fe at 1 bar) confirming the positive effect of alkali metals on the steady-state fraction of Fe_5C_2 in CO_2–FT (Figure 6b).[55–56] A significant decrease in the rate with rising pressure was found for all samples (Figure 5b,c), which could be due to the stability of FeO at higher pressures.

Conclusions

The present study demonstrates the potential of the time-resolved in situ XAS method, combined with the kinetic analysis of the results obtained, to provide the fundamentals of the formation of Fe_5C_2 from FeC_2O_4 promoted by an alkali metal (Li, Na, K, Rb, or Cs) at 350 °C under CO_2 Fischer-Tropsch conditions. The precursor was obtained by dehydration of $FeC_2O_4{\cdot}2H_2O$ during heating to 350 °C in He. In contrast to the decomposition of FeC_2O_4 in oxidizing, reducing or inert atmospheres, FeO can be stabilized at 350 °C using a $H_2/CO_2 = 3$ reaction feed. The primarily formed FeO is consequently converted to Fe_5C_2 via Fe_3C carbide. Both processes slowed down when the reaction pressure increased from 1 to 7.5 bar. This was explained by the stabilization of FeO at higher partial pressures of water steam.

A kinetics-constrained neural ODE approach was proven to provide mechanistic and kinetic insights into the formation of FeO and Fe_5C_2 in comparison with a classical Johnson–Mehl–Avrami–Erofeev–Kolmogorov model, which can be applied for the first process only. Both approaches suggest that the conversion of FeC_2O_4 to FeO at 1 bar occurs according to a nucleation mechanism, while a diffusion-controlled mechanism prevails at higher pressures. The change in mechanism was explained by an improvement in the stability of FeO, which may lead to the encapsulation of FeC_2O_4 resulting in diffusion limitations during the decomposition process.

Regardless of the pressure, the formation of iron carbides from FeO follows the diffusion mechanism. The initial rate of this reaction is accelerated in the presence of an alkali metal promoters but hindered with increasing pressure.

Experimental Section

Samples Preparation

The catalysts were prepared through incipient wetness impregnation of commercial ferrous oxalate dihydrate ($FeC_2O_4{\cdot}2H_2O$, Sigma Aldrich, 99 %) with an aqueous solution of alkali metal (Li, Na, K, Rb or Cs) carbonate as described in Ref. [30]. The promoted samples were dried at 110 °C for 24 h. No additional thermal treatments were performed.

In Situ X-ray Absorption Spectroscopy

X-ray absorption near-edge structure (XANES) and extended X-ray absorption fine structure (EXAFS) spectra at the Fe K absorption edge (7112 eV) were recorded at the P65 beamline of the PETRA III synchrotron (DESY, Hamburg) in transmission mode. The energy of the X-ray photons was selected by a Si (111) double-crystal monochromator and the beam size was set by means of slits to 0.2 (vertical) × 1.5 (horizontal) mm^2. The samples were diluted with boron nitride (10 wt.% of $FeC_2O_4{\cdot}2H_2O$ in BN), sieved into a fraction of 100–200 μm and were loaded in an in situ micro-reactor (quartz capillary, 1.5 mm diameter, 0.02 mm wall thickness). The total amount of each sample was about 0.5 mg. The catalysts were initially heated to 350 °C at 1 bar in a flow of He (20 ml/min flow rate, 5 °C/min heating rate). Hereafter, He was replaced by a CO_2:H_2 = 1:3 mixture (20 ml/min flow rate). The XANES spectra were measured for 2 hours at 1 bar and 350 °C. Additional experiments were performed at 7.5 bar. The pressure was increased after reaching 350 °C at ambient pressure and changing to CO_2:H_2 = 1:3 mixture. The XANES spectra were normalized, and the EXAFS spectra background was subtracted using the ATHENA program from the IFFEFIT software package.[57] A linear combination analysis of the XANES spectra was performed in the energy range from -15 eV to $+40$ eV with respect to the absorption edge. The k^2-weighted EXAFS functions were Fourier transformed (FT) in the k range of 3.0–10.0 $Å^{-1}$ for samples measure at room temperature and 2.0-8.0 $Å^{-1}$ for in situ measurements at higher temperature. The principal component analysis (PCA) was used to identify the number of independent compounds in XANES data. To extract the correct number of the components that have real physical/chemical meaning, the scree plot[39–40] and factor indicator function (IND) suggested by Malinowski[41] were used. The scree plot illustrates the relationship between eigenvalues and component numbers. At first, the eigenvalues decrease sharply, followed by a more gradual decline (see Figure S9). The components associated with the initial steep drop typically have physical meaning, while those beyond the "elbow" mainly represent noise and contribute minimally to the data set.[39] The IND function was estimated by the following formula:[41]

$$IND(N) = \frac{1}{(n-N)^2}\sqrt{\frac{\sum_{i=N+1}^{n}\lambda_i}{m(n-N)}}, \tag{5}$$

where N is the component number; n is the number of spectra; m is the dimension of spectra; λ_i – the eigenvalue for principal component i. The IND function reaches a minimum when the correct component number of components is employed.[39] In addition, the analysis of the number of correct components was performed by fitting XANES spectra using linear combinations of different numbers/types of reference spectra. Non-negative linear regression from SciPy[42] was applied to determine the regression coefficients and the corresponding residuals. The mean residual value across all spectra was used as the loss function (separately for 1 and 7.5 bar data).

Kinetic Modeling

To derive kinetic parameters of FeC_2O_4 transformations under CO_2-FT conditions, we used both a classical approach for analyzing topochemical (solid-state) reactions and artificial neural networks. The rate of a topochemical reaction can be presented by equation 6 according to previous studies.[54, 58–59]

$$\frac{d\alpha}{dt} = k(T, p_1, \ldots p_n)\cdot f(\alpha) \tag{6}$$

where α– the conversion of the reacting compound; t– the reaction time; k – the effective reaction rate constant; p_i – the partial pressure of gas phase component i; $f(\alpha)$ – the function describing the conversion mechanism.

One of frequently used models to describe solids crystallization kinetics is a Johnson–Mehl–Avrami–Erofeev–Kolmogorov (JMAEK) model,[48, 60–63] for which $f(\alpha)$ is presented as:

$$f(\alpha) = n(1-\alpha)(-\ln(1-\alpha))^{1-\frac{1}{n}} \tag{7}$$

where n– the Avrami exponent, where value gives the information about mechanism of reaction.

The JMAEK model can also be represented in the integral form by equation 8. This equation can be represented in a linear form also known as the Sharp-Hancock plot (equation 9). It was used for estimating the reaction rate constant k and the Avrami exponent n from the experimental data in the α range between 0.2 and 0.8 for 1 bar and 0.35 and 0.65 for 7.5 bar representing a linear section with a sufficient number of points. It is known that the reaction constant k correlates with the $f(\alpha)$

function and the reaction mechanism.[54] Accordingly, to understand whether and how the kind of alkali metal promoter affects the kinetics of ferrous oxalate decomposition, the k and n values obtained from the fit were further used for calculating the rates of ferrous oxalate decomposition at α of 0.50 conversion using equations 6 and 7.

$$\alpha = 1 - e^{-(kt)^n} \tag{8}$$

$$\ln[-\ln(1-\alpha)] = n\ln(t) + n\ln(k) \tag{9}$$

Due to the complexity of multi-steps reaction modeling, in addition to the above analysis, kinetic-constrained neural ordinary differential equations (ODEs) were applied to describe the process of ferrous oxalate decomposition.[64] The key idea of this method is to integrate the general knowledge about the process into the architecture of the neural ODE. In our case, we used the information that the reaction rate should be proportional to the molar fraction of ferrous oxalate. The rate would be equal to zero in its absence. It was also assumed that there are two reactions involved in the conversion of FeC_2O_4, i.e., FeC_2O_4 to FeO followed by FeO to iron carbide (Fe_xC_y). To simplify the model, the formation of Fe_3O_4 at 7.5 bar was not considered and the fraction of Fe_3O_4 was added to FeO fraction as total oxide phase. The fractions of Fe_3C and Fe_5C_2 were summed as one iron carbide phase (Fe_xC_y). The following kinetic equations were used to describe the rates of two reactions:

$$r_1 = k_1 \cdot x_1 \cdot f_1(d) \tag{10}$$

$$r_2 = k_2 \cdot x_2 \cdot f_2(d) \tag{11}$$

where r_i is the rate of reaction i; k_i is the i-reaction rate constant; x_1, x_2 are the molar fractions of FeC_2O_4 and FeO, respectively; $f_i(\mathbf{d})$– i-output of the feedforward artificial neural network defined by the function $f(\mathbf{d})$; $\mathbf{d}$ – the vector of descriptors (inputs for neural network), which are different for different models.

Based on equations 10 and 11 the temporal changes in the molar fractions of FeC_2O_4 (x_1), FeO (x_2) and Fe_xC_y (x_3) can be represented by the following system of ODEs.

$$\frac{dx_1}{dt} = -r_1 \tag{12}$$

$$\frac{dx_2}{dt} = r_1 - r_2 \tag{13}$$

$$\frac{dx_3}{dt} = r_2 \tag{14}$$

Three different kinetics-constrained neural ODE models were used, which differ in the kind of descriptors, the vector d. Its architectures are presented in the Figure 7.

In the first model (M−1), the mechanism for both reactions was assumed to only depend on the molar fraction of the initial solid reactant, i.e., FeC_2O_4 and FeO participating in reactions 1 and 2, respectively. The corresponding general neural network $f(\mathbf{d})$ was represented as two merged feedforward neural networks, each with only one input (x_1 and x_2, respectively) and one output (see Figure 7). These outputs were used as outputs for the general neural network as $f_1(\mathbf{d})$ and $f_2(\mathbf{d})$ for equations 10 and 11, respectively. In the second model (M−2), the mechanisms of both reactions depend on the fractions of FeC_2O_4 and FeO. Thus, the neural network of this model has two inputs: x_1, x_2 as well as two outputs (see Figure 7). It is worth noting that the influence of the promoters (alkali metals) on the reaction mechanism was neglected in both M−1 and M−2 models since only the molar fraction of iron compounds was used as inputs of the respective neural networks. Thus, all samples differ only in the values of the rate constants which are being varied during data fitting. It is important to say that such architecture of the neural networks in models M−1 and M−2 suggests that the mechanism of decomposition of FeC_2O_4 and FeO is the same for all samples and, thus, does not depend on the presence/nature of alkali metals. The latter effects are considered in the model M−3. It has the following inputs: x_1, x_2, and $\mathbf{d_n}$ (see Figure 7). The latter is the vector (d_{Fe}, d_{Li}, d_{Na}, d_K, d_{Rb}, d_{Cs}) where d_i – is 1 if the oxalate was promoted with i-dopant (d_{Fe} is 1 means unpromoted ferrous oxalate). For example, (0, 0, 1, 0, 0, 0) means the vector of the material promoted with Na.

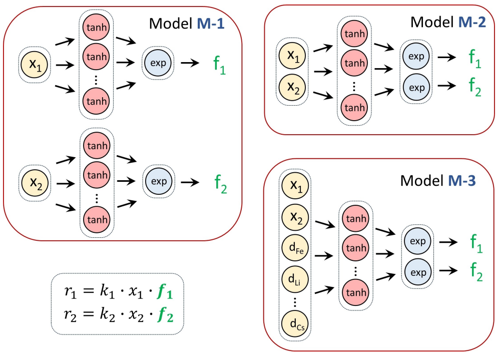

Figure 7. The architectures of M-1, M-2 and M-3 kinetics-constrained neural ODE models.

The feedforward neural networks have 1 hidden layer (10 nodes) with a hyperbolic tangent activation function and one output layer (2 nodes for reactions 1 and 2) with an exponential activation function. A 5th order Runge-Kutta method for the Dormand-Prince-Shampine (DOPRI5) method was used for the integration of neural ODE according to [65]. The following loss function was used for training the neural ODE models:

$$loss = \frac{1}{n}\sum_{i=1}^{n}\left(x_i^{exp} - x_i^{pred}\right)^2 \tag{15}$$

where n – the number of experimental points; x_i^{exp} – the experimental molar fraction of compound i; x_i^{pred}– the molar fraction of compound i predicted with the neural ODE model. Training was carried out by minimizing the loss functions using the ADAM optimizer[66] with a learning rate of 0.005 and was terminated when the loss function flattened out. L_2-regularization was used to reduce the stiffness of the neural ODE during training. The regularization parameter was set to 10–6. Mean absolute error (MAE) was used to compare the generalization of the neural ODE models which was defined as:

$$MAE = \frac{1}{n}\sum_{i=1}^{n}\left|x_i^{exp} - x_i^{pred}\right| \tag{16}$$

Acknowledgments

This work was funded by the Deutsche Forschungsgemeinschaft (DFG) under the priority program SPP 2080 (grant nos. KO 2261/10-1, KO 2261/10-2, BR 1380/29-2). The XAS experiments were carried out at PETRA III of DESY (Hamburg, Germany), a member of the Helmholtz Association HGF, and we would like to thank Dr. Edmund Welter for their assistance in using beamline P65 (proposal I-20230372). The authors thank Dr. Dan Zhao, Dr. Qiyang Zhang and Lorena Baumgarten for their assistance during the XAS measurements. We thank the Federal German Ministry for Education and Research (BMBF) for funding the EELS spectrometer in the frame of project ESMAC. Open Access funding enabled and organized by Projekt DEAL.

Conflict of Interests

The authors declare no conflict of interest.

Data Availability Statement

All the data are openly available on Repo4Cat in [37] via the link: https://hdl.handle.net/21.11165/4cat/638s-k9dx.

Keywords: In situ XAS · Ferrous oxalate · CO_2Fischer Tropsch · Iron carbide · Alkali metals

[1] V. Carles, P. Alphonse, P. Tailhades, A. Rousset, *Thermochim. Acta* **1999**, *334*, 107–113.
[2] D. Smrčka, V. Procházka, P. Novák, J. Kašlík, V. Vrba, in *Mössbauer spectroscopy in materials science 2016* Vol. 1781, AIP Publishing, Slovakia, **2016**.
[3] M. Hermanek, R. Zboril, M. Mashlan, L. Machala, O. Schneeweiss, *J. Mater. Chem.* **2006**, *16*, 1273–1280.
[4] M. K. Gnanamani, H. H. Hamdeh, W. D. Shafer, S. D. Hopps, B. H. Davis, *Appl. Catal. A* **2018**, *564*, 243–249.
[5] S. Cariç, L. Marinkov, J. Slivka, *Phys. Status Solidi* **1975**, *31*, 263–268.
[6] E. J. Baran, *Geochemistry* **2016**, *76*, 449–460.
[7] E. D. Macklen, *J. Inorg. Nucl. Chem.* **1967**, *29*, 1229–1234.
[8] Y. Jia, J. Ni, F. Fang, *Mater. Sci. Semicond. Process.* **2021**, *125*, 105650.
[9] V. Rao, A. L. Shashimohan, A. B. Biswas, *J. Mater. Sci.* **1974**, *9*, 430–433.
[10] B. Boyanov, D. Khadzhiev, V. Vasilev, *Thermochim. Acta* **1985**, *93*, 89–92.
[11] G. C. Nicholson, *J. Inorg. Nucl. Chem.* **1967**, *29*, 1599–1604.
[12] A. S. Skrypnik, S. A. Petrov, V. A. Kondratenko, Q. Yang, H. Lund, A. A. Matvienko, E. V. Kondratenko, *ACS Catal.* **2022**, *12*, 11355–11368.
[13] R. Zboril, L. Machala, M. Mashlan, M. Hermanek, M. Miglierini, A. Fojtik, *Phys. Status Solidi* **2004**, *1*, 3583–3588.
[14] P. Santawaja, S. Kudo, A. Mori, A. Tahara, S. Asano, J.-i. Hayashi, *ACS Sustainable Chem. Eng.* **2020**, *8*, 13292–13301.
[15] R. A. Brown, S. C. Bevan, *J. Inorg. Nucl. Chem.* **1966**, *28*, 387–391.
[16] K. Nomura, Y. Ujihira, *J. Anal. Appl. Pyrolysis* **1983**, *5*, 221–236.
[17] R. Majumdar, P. Sarkar, U. Ray, M. Roy Mukhopadhyay, *Thermochim. Acta* **1999**, *335*, 43–53.
[18] M. R. Anantharaman, S. S. Shewale, V. S. Rao, K. Seshan, H. V. Keer, *Indian J. Chem.* **1982**, *21 A*, 990–992.
[19] P. Dong, H. Liang, J. Liu, K. Wei, J. Zhao, X. Li, Y. Zhang, *Metall. Res. Technol.* **2017**, *114*, 515.
[20] K. S. Rane, A. K. Nikumbh, A. J. Mukhedkar, *J. Mater. Sci.* **1981**, *16*, 2387–2397.
[21] Y. Kong, D. Xue, F. Li, *Phys. Status Solidi* **1996**, *154*, 553–558.
[22] A. S. Skrypnik, Q. Yang, A. A. Matvienko, V. Y. Bychkov, Y. P. Tulenin, H. Lund, S. A. Petrov, R. Kraehnert, A. Arinchtein, J. Weiss, A. Brueckner, E. V. Kondratenko, *Appl. Catal. B* **2021**, *291*, 120121.
[23] A. S. Skrypnik, S. A. Petrov, V. A. Kondratenko, Q. Yang, A. A. Matvienko, E. V. Kondratenko, *J. Catal.* **2023**, *425*, 286–295.
[24] Ramani, M. P. Sathyavathiamma, N. G. Puttaswamy, R. M. Mallya, *Phys. Status Solidi* **1983**, *77*, 87–96.
[25] D. Ye, W. Tang, T. Zhang, L. Lv, Z. Zou, R. K. Gupta, S. Tang, *Colloids Surf. A* **2022**, *654*, 130145.
[26] S. Najari, S. Saeidi, A. Sápi, Á. Szamosvölgyi, Á. Papp, A. Efremova, H. Bali, Z. Kónya, *Chem. Eng. J.* **2024**, *485*, 149787.
[27] H. Qi, W. Si, Z. Xu, G. Wang, X. Liu, C. Lyu, B. Huang, N. Tsubaki, C. Xing, J. Sun, *ChemSusChem* **2024**, *n/a*, e202400484.
[28] S. Pérez, F. Mondragón, A. Moreno, *Appl. Catal. A* **2019**, *587*, 117264.
[29] X. Yang, H. Zhang, Y. Liu, W. Ning, W. Han, H. Liu, C. Huo, *Catalysts* **2019**, *9*, 347.
[30] A. S. Skrypnik, H. Lund, Q. Yang, E. V. Kondratenko, *Catal. Sci. Technol.* **2023**, *13*, 4353–4359.
[31] S. Y. Hong, D. H. Chun, J.-I. Yang, H. Jung, H.-T. Lee, S. Hong, S. Jang, J. T. Lim, C. S. Kim, J. C. Park, *Nanoscale* **2015**, *7*, 16616–16620.
[32] J. Liu, A. Zhang, X. Jiang, M. Liu, J. Zhu, C. Song, X. Guo, *Ind. Eng. Chem. Res.* **2018**, *57*, 9120–9126.
[33] J. Liu, G. Zhang, X. Jiang, J. Wang, C. Song, X. Guo, *Catal. Today* **2021**, *371*, 162–170.
[34] M. Wilke, F. O. Farges, P.-E. Petit, G. E. Brown, Jr., F. O. Martin, *Am. Mineral.* **2001**, *86*, 714–730.
[35] A. Kuzmin, J. Chaboy, *IUCrJ* **2014**, *1*, 571–589.
[36] C. Yang, H. Zhao, Y. Hou, D. Ma, *J. Am. Chem. Soc.* **2012**, *134*, 15814–15821.
[37] E. A. Fedorova, A. Fedorov, D. E. Doronkin, D. Linke, C. Kubis, A. Brückner, E. V. Kondratenko, NFDI4Cat Central Data Repository, 2025. https://hdl.handle.net/21.11165/4cat/638s-k9dx.
[38] S. Beauchemin, D. Hesterberg, M. Beauchemin, *Soil Sci. Soc. Am. J.* **2002**, *66*, 83–91.
[39] A. Martini, E. Borfecchia, *Crystals* **2020**, *10*.
[40] A. Manceau, M. Marcus, T. Lenoir, *J. Synchrotron Radiat.* **2014**, *21*, 1140–1147.
[41] E. R. Malinowski, *Factor Analysis in Chemistry*, 3 ed., John Wiley & Sons, Nashville, TN, **2002**.
[42] P. Virtanen, R. Gommers, T. E. Oliphant, M. Haberland, T. Reddy, D. Cournapeau, E. Burovski, P. Peterson, W. Weckesser, J. Bright, S. J. van der Walt, M. Brett, J. Wilson, K. J. Millman, N. Mayorov, A. R. J. Nelson, E. Jones, R. Kern, E. Larson, C. J. Carey, İ. Polat, Y. Feng, E. W. Moore, J. VanderPlas, D. Laxalde, J. Perktold, R. Cimrman, I. Henriksen, E. A. Quintero, C. R. Harris, A. M. Archibald, A. H. Ribeiro, F. Pedregosa, P. van Mulbregt, A. Vijaykumar, A. P. Bardelli, A. Rothberg, A. Hilboll, A. Kloeckner, A. Scopatz, A. Lee, A. Rokem, C. N. Woods, C. Fulton, C. Masson, C. Häggström, C. Fitzgerald, D. A. Nicholson, D. R. Hagen, D. V. Pasechnik, E. Olivetti, E. Martin, E. Wieser, F. Silva, F. Lenders, F. Wilhelm, G. Young, G. A. Price, G.-L. Ingold, G. E. Allen, G. R. Lee, H. Audren, I. Probst, J. P. Dietrich, J. Silterra, J. T. Webber, J. Slavič, J. Nothman, J. Buchner, J. Kulick, J. L. Schönberger, J. V. de Miranda Cardoso, J. Reimer, J. Harrington, J. L. C. Rodríguez, J. Nunez-Iglesias, J. Kuczynski, K. Tritz, M. Thoma, M. Newville, M. Kümmerer, M. Bolingbroke, M. Tartre, M. Pak, N. J. Smith, N. Nowaczyk, N. Shebanov, O. Pavlyk, P. A. Brodtkorb, P. Lee, R. T. McGibbon, R. Feldbauer, S. Lewis, S. Tygier, S. Sievert, S. Vigna, S. Peterson, S. More, T. Pudlik, T. Oshima, et al., *Nat. Methods* **2020**, *17*, 261–272.
[43] D. Bruce, P. Hancock, *Br. Corros. J.* **1969**, *4*, 221–222.
[44] J. Zieliński, I. Zglinicka, L. Znak, Z. Kaszkur, *Appl. Catal. A* **2010**, *381*, 191–196.
[45] L. Braun, J. Spielmann, D. E. Doronkin, C. Kuhn, A. Maliugin, D. I. Sharapa, I. Huck, J. Bao, S. Tischer, F. Studt, O. Deutschmann, U. I. Kramm, J.-D. Grunwaldt, *ChemSusChem* **2024**, e202401045.
[46] A. J. Norquist, D. O'Hare, *J. Am. Chem. Soc.* **2004**, *126*, 6673–6679.

[47] C. Morey, Q. Tang, S. Sun, K. Huang, *J. Electrochem. Soc.* **2023**, *170*, 104504.
[48] K. Dimitra, C. Konstantinos, *Thermochim. Acta* **2021**, *704*, 179030.
[49] K. Piotrowski, K. Mondal, T. Wiltowski, P. Dydo, G. Rizeg, *Chem. Eng. J.* **2007**, *131*, 73–82.
[50] Q. Tang, K. Huang, *Chem. Eng. J.* **2022**, *434*, 134771.
[51] J. Li, X. Cheng, C. Zhang, J. Wang, W. Dong, Y. Yang, Y. Li, *J. Chem. Technol. Biotechnol.* **2017**, *92*, 1472–1480.
[52] D. Wang, Z. Xie, M. D. Porosoff, J. G. Chen, *Chem* **2021**, *7*, 2277–2311.
[53] J. S. Jestilä, J. K. Denton, E. H. Perez, T. Khuu, E. Aprà, S. S. Xantheas, M. A. Johnson, E. Uggerud, *Phys. Chem. Chem. Phys.* **2020**, *22*, 7460–7473.
[54] A. Khawam, D. R. Flanagan, *J. Phys. Chem. B* **2006**, *110*, 17315–17328.
[55] Y. Yang, H. Zhang, H. Ma, W. Qian, Q. Sun, W. Ying, *Fuel* **2022**, *326*, 125090.
[56] P. S. Sai Prasad, J. W. Bae, K.-W. Jun, K.-W. Lee, *Catal. Surv. Asia* **2008**, *12*, 170–183.
[57] B. Ravel, M. Newville, *J. Synchrotron Radiat.* **2005**, *12*, 537–541.
[58] A. Khawam, D. R. Flanagan, *J. Pharm. Sci.* **2006**, *95*, 472–498.
[59] S. Vyazovkin, *Int. Rev. Phys. Chem.* **2020**, *39*, 35–66.
[60] W. Johnson, R. Mehl, *Trans. Metall. Soc. AIME* **1939**, *135*, 416–442.
[61] M. Avrami, *J. Chem. Phys.* **1940**, *8*, 212–224.
[62] B. Erofe'ev, *Compt Rend Acad Sci USSR* **1946**, *52*, 511–514.
[63] A. A. Kolmogorov, *Bull Acad Sci* **1937**, *1*, 355–359.
[64] A. Fedorov, A. Perechodjuk, D. Linke, *Chem. Eng. J.* **2023**, *477*, 146869.
[65] M. Poli, S. Massaroli, A. Yamashita, H. Asama, J. Park, *arXiv:2009.09346* **2020**.
[66] D. P. Kingma, J. Ba, *arXiv:1412.6980* **2014**.

Manuscript received: October 15, 2024
Version of record online: ■■, ■■